JACS
JOURNAL OF THE AMERICAN CHEMICAL SOCIETY
Article
pubs.acs.org/JACS

Targeted Synthesis of Silicomolybdic Acid (Keggin Acid) inside Mesoporous Silica Hollow Spheres for Friedel−Crafts Alkylation

Jian Dou[†] and Hua Chun Zeng*[,†,‡]

[†]Department of Chemical and Biomolecular Engineering, Faculty of Engineering, National University of Singapore, 10 Kent Ridge Crescent, Singapore 119260

[‡]Institute of Materials Research and Engineering (IMRE), 3 Research Link, Singapore 117602

Ⓢ *Supporting Information*

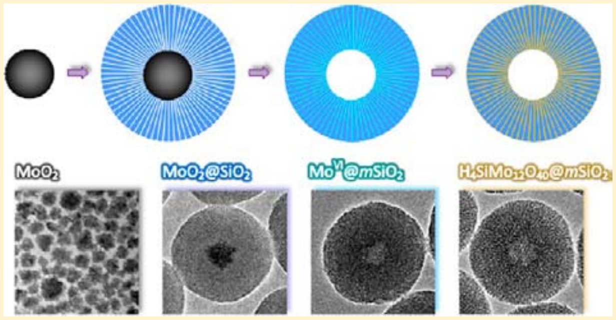

ABSTRACT: Herein we report an *inside-out* preinstallation-infusion-hydration method for targeted synthesis of Keggin heteropoly acids (silicomolybdic acid, $H_4SiMo_{12}O_{40}$) within mesoporous silica (SiO_2) hollow spheres. In this process, discrete molybdenum dioxide (MoO_2) nanoparticles with diameter size ranging from 25 to 60 nm were first prepared by a one-pot hydrothermal route in water/ethanol mixed solvents at 180 °C, which were then used as cores to grow the shell of supramolecular templated silica with tetraethyl orthosilicate (TEOS) and hexadecyltrimethyl- ammonium chloride (CTACl) in alkaline solution. By thermal treatment of as-synthesized $MoO_2@SiO_2$ core−shell spheres, the organic template was burned off and mesoporous shell was formed (BET specific surface area was as high as 872 m^2/g). Meanwhile, the encapsulated MoO_2 was oxidized to Mo^{6+} and infused to the mesoporous silica shells, forming heptamolybdate species ($Mo_7O_{24}^{6-}$) uniformly dispersed on the mesopore surfaces of silica, while generating void space at the center of spheres. After hydration with water, $H_4SiMo_{12}O_{40}$ was formed by reaction between the surface $Mo_7O_{24}^{6-}$ and silica species in the presence of water. The prepared $H_4SiMo_{12}O_{40}$ @ $m$$SiO_2$ hollow spheres were tested for Friedel−Crafts alkylation of toluene by benzyl alcohol. The $H_4SiMo_{12}O_{40}@mSiO_2$ catalysts fabricated via this novel route exhibited excellent catalytic activity toward benzylation of toluene, which was approximately 2.6 times as high as that of commercial Amberlyst-15 catalyst. In addition, the $H_4SiMo_{12}O_{40}@mSiO_2$ catalyst was very robust and could be reused after regeneration.

■ INTRODUCTION

Mesoporous silica materials have received tremendous research interest and activity over the last two decades since the discovery of MCM-type of mesoporous silica in 1990s.[1−3] Owing to their uniform pore size, ordered pore structures, and high surface areas, mesoporous silica has numerous potential applications across a wide variety of fields such as separation, sorption, controlled release, biosensing, heterogeneous catalysis, etc.[4−9] Accordingly, much effort has been devoted to preparing mesoporous silica with variations of pore structure, surface area, composition, interior space, and exterior morphology. For instance, incorporation of inorganic or organic components into the mesoporous silica structures has been persistently pursued in order to develop novel composite materials for drug delivery as well as catalytic applications.[6−9] Through compositional modification of this type of composites or supports, unprecedented physicochemical properties could be attained.[4−9] There are basically three strategies available to prepare inorganic or organic mesoporous silica composites. The first one is by co-condensation of inorganic/organic precursors with a silica source, which could yield composite materials with homogeneous composition.[10] However, there could be a limitation on the maximum amount of inorganic materials loaded due to lack of hydrolyzable precursors. The second method is through postmodification with impregnation or surface reaction, from which inorganic/organic materials are deposited/grafted on the surfaces of mesoporous silica though the uniformity could be an issue.[11] The third approach through preinstallation is quite commonly used for synthesis of core−shell and yolk−shell structures,[12−16] but their mesopores or interior spaces are not utilized fully as supports for inorganic and organic materials.

In addition to the above functionalization, miniaturization and shape-controlled preparation of mesoporous silica have also attracted significant research attention.[17,18] In particular, hollow nanostructures have been considered in recent years as promising nanomaterials for a wide range of applications.[19−22] In this regard, for example, void space within mesoporous silica spheres can function as a nanoreactor for catalytic reaction or as a nanocontainer for controlled-release application.[12,23] Compared to mesoporous bulk silica, furthermore, such hollow spheres will render the thickness of silica shells within nanometer scale, which is highly desirable for mass transfer

Received: June 8, 2012
Published: September 5, 2012

dx.doi.org/10.1021/ja3055723 | *J. Am. Chem. Soc.* 2012, 134, 16235−16246

of reactants and products especially for liquid-phase reactions. Due to shorter pore channels and thus less traveling blockage, the surface of mesopores in the shell structure can be utilized more efficiently when these hollow spheres are used as catalyst supports. Many approaches have been reported in the literature.[24−30] For example, soft templates such as emulsions, vesicles, and gas bubbles have been employed, which generally yield hollow mesoporous silica spheres with a relatively wide size distribution.[24−27] On the other hand, hard templates such as polymer beads with uniform sizes are also widely adopted, which give rise to hollow mesoporous silica spheres with a remarkably narrow size distribution, although the templates have to be removed by extraction or calcinations.[28,29] Other so-called template-free methods through Ostwald ripening or chemical etching to form hollow structures have also been developed.[12,30]

Because it is a weak acidic oxide, silica also is very suitable to serve as a catalyst support for solid acids.[31] In this work, therefore, we choose acid-catalyzed Friedel−Crafts alkylation as a model reaction for the present investigation, as it is an important industry process to produce diphenyl compounds which are essential intermediates for pharmaceutical and fine chemical production.[32] Conventionally, Friedel−Crafts alkylation is catalyzed by homogeneous acids such as $AlCl_3$, $FeCl_3$, $ZnCl_2$, and H_2SO_4 that are very active, but a large amount of process wastes is also generated unavoidably.[31] Additionally, it is very difficult to recover the catalysts from the reaction mixture. Hence, considerable efforts have been made to develop environmentally benign, recyclable, heterogeneous solid acid catalysts such as zeolites, clays, heteropoly acids, ion-exchanged polymers, sulfated metal oxide and carbon as well as other oxides and mixed oxides.[33−40] Moreover, mesoporous zeolites have received intense research interests due to their strong acidity and mesoporous structure which can accommodate large reactant molecules.[41−46]

Among the above heterogeneous catalysts, heteropoly acids are known to be very strong solid acids and have wide applications in catalysis.[39,47] It is noted that acidity of solid heteropoly acids is even stronger than conventional solid acids such as zeolites X and Y.[39,47] As bulk heteropoly acids typically have a very low surface area (1−5 m^2/g), it is preferable to prepare heteropoly acids on high surface area catalyst supports such as mesoporous silica (i.e., MCM-41 and SBA-15).[48−55] There are two strategies that have been developed to prepare silica-supported heteropoly acids. The first method is to impregnate mesoporous silica with heteropoly acids.[48−51] Though it is simple for this *outside-in* process, nevertheless, pore blockage and thus less working-surface catalyst could be a major process drawback. The second method is to include heteropoly acids within mesoporous silica through sol−gel synthesis, which can ensure homogeneous dispersion of mesoporous silica within mesoporous silica matrix, minimizing pore blockage.[52−55] However, the supramolecular template in the latter has to be removed by either solvent extraction or thermal treatment above 400 °C, which may result in leaching or decomposition of heteropoly acids. It is known that many heteropoly acids have high solubility in polar solvents and start decomposing above 400 °C.[39,52,56−58] It is noted that silica encapsulation followed by thermal treatment has been utilized for controllable transformation of nanaparticles@silica nanostructures to achieve hollowed metal oxides, heterodimers/alloy nanoparticles, and highly dispersed metals/metal oxides on silica support for biomedical, catalytic and magnetic applications.[59−61] To overcome the difficulties and dilemmas encountered in the above methods to prepare supported heteropolyacids, in this contribution, we have developed a preinstallation−infusion−hydration (*inside-out*) method to prepare highly dispersed silicomolybdic acid ($H_4SiMo_{12}O_{40}$) within mesoporous hollow spheres of silica, as depicted in Figure 1. First, discrete MoO_2 nanoparticles are prepared by hydrothermal synthesis. The as-synthesized MoO_2 nanoparticles are then used as cores to form MoO_2@SiO_2 core−shell spheres. Next, thermal treatment of MoO_2@SiO_2 core−shell spheres leads to oxidation and infusion of encapsulated MoO_2 core nanoparticles, which results in highly dispersed heptamolybdate species ($Mo_7O_{24}^{6-}$) within mesoporous silica shells and at the same time forms hollow mesoporous silica spheres. Finally, hydration of the as-prepared Mo^{VI}@*m*SiO_2 hollow spheres generates silicomolybdic acid ($H_4SiMo_{12}O_{40}$) which is highly dispersed within the mesoporous silica shells. Because this is an *inside-out* synthesis for catalysts, blockage in the pore entrance can be avoided compared to other conventional preparative methods such as the metal−salt impregnation technique by which catalytic components are introduced to the existing mesopores via *outside-in* processes. The resultant $H_4SiMo_{12}O_{40}$ @*m*SiO_2 has been elucidated to be an active, robust, solid acid catalyst for Friedel−Crafts alkylation.

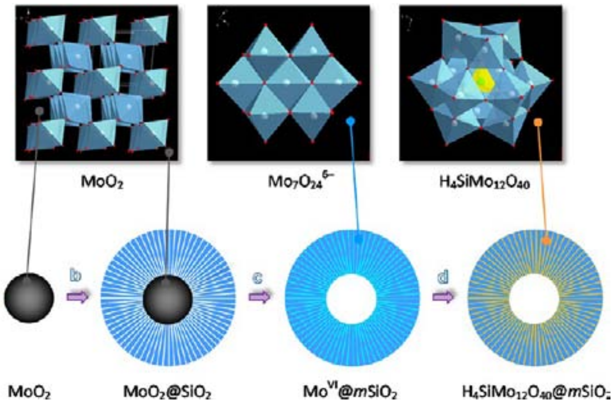

Figure 1. Schematic flowchart of targeted synthesis of silicomolybdic acid ($H_4SiMo_{12}O_{40}$) inside silica hollow spheres: (a) synthesis of MoO_2 nanoparticles, (b) deposition of silica shell on the MoO_2 core, (c) thermal infusion of MoO_2 into silica mesopores (during which MoO_2 was oxidized to MoO_3 and then to $Mo_7O_{24}^{6-}$), and (d) hydration of Mo^{VI}@*m*SiO_2 to $H_4SiMo_{12}O_{40}$@*m*SiO_2. Notations of crystallographic structures of MoO_2, $Mo_7O_{24}^{6-}$, and $H_4SiMo_{12}O_{40}$: the white, red, and green spheres represent molybdenum, oxygen, and silicon atoms, respectively (hydrogen atoms are not shown). The sky-blue octahedral unit represents MoO_6, and the yellow tetrahedral unit signifies SiO_4.

■ EXPERIMENTAL SECTION

Preparation of MoO_2 Nanoparticles. Discrete MoO_2 nanoparticles with sizes in the range of 25−60 nm were obtained by a simple one-pot hydrothermal synthesis. Briefly, 150 mg of ammonium heptamolybdate (AHM, Merck) was dissolved in 22.0 mL of deionized water, followed by addition of 10 mL of ethanol (Merck). Later, 500 mg of polyvinyl-pyrrolidone (PVP; K-40, Aldrich) was added to the above solution. The resulted mixture was stirred at room temperature for 30 min. Afterward, the solution was transferred to a Teflon-lined stainless steel autoclave (40 mL capacity), and hydrothermally treated in an electric oven at 180 °C for 16 h. The autoclave was then cooled under tap water, and dark precipitate (i.e., product MoO_2 nanoparticles) was harvested by centrifugation and washed with ethanol−acetone cosolvent for four times. In addition, MoO_2 nanoparticles with a smaller size (∼20 nm) could also be synthesized by adding 1.0 mL of 1.0 M HCl into the above synthesis mixture while other parameters remained unchanged.

Preparation of MoO_2@SiO_2 Core−Shell Spheres. The above synthesized MoO_2 nanoparticles were used as cores to coat with mesoporous silica shells by hydrolysis and condensation of tetraethyl orthosilicate (TEOS, Aldrich) in water/ethanol mixed solvent by a literature method with some modifications.[17] In a typical synthesis, for instance, 5, 10, 20, 30, and 40 mg of the MoO_2 nanoparticles synthesized above was redispersed respectively in a mixed solvent prepared from 33 mL of deionized water and 20.0 mL of ethanol by sonication for 30 min. After that, 0.55 mL of 25% hexadecyltrimethylammonium chloride (CTACl, Sigma-Aldrich) and 0.2 mL of triethanolamine (TEA, Acros Organics; to provide a basic environment) were added to the above mixture and well stirred at room temperature for another 30 min, followed by a dropwise addition of 0.4 mL of TEOS. The resultant mixture was further stirred for 16 h at room temperature before separating solid, dark precipitates *via* centrifugation. The obtained products (MoO_2@SiO_2) were washed with acetone and ethanol and dried in an oven at 80 °C overnight.

Preparation of Mo^{VI}@*m*SiO_2 Hollow Spheres. The above-obtained MoO_2@SiO_2 core−shell precursors were calcined in an electric furnace with laboratory air at 550 °C for 6 h to remove the organic template, from which the gel precursor (i.e., SiO_2) shells were converted into thermally stabilized mesoporous silica (i.e., *m*SiO_2). At the same time, the encapsulated MoO_2 cores were oxidized into MoO_3; this process was shown with the color change from the dark MoO_2@SiO_2 precursor to white products. The obtained white products were denoted as Mo^{VI}@*m*SiO_2-*X*, where $X = 10$, 20, 30, and 40; the number corresponds to the amount (weight in mg) of MoO_2 nanoparticles used in the above synthesis of MoO_2@SiO_2 core−shell nanospheres. Depending on the *X* value, different Mo^{VI} species or phases were formed in this thermal oxidative conversion, which will be detailed in the respective parts of this article.

Preparation of $H_4SiMo_{12}O_{40}$@*m*SiO_2 Hollow Spheres. The $H_4SiMo_{12}O_{40}$@*m*SiO_2 was prepared by immersing the above synthesized Mo^{VI}@*m*SiO_2 (e.g., 100 mg) into deionized water (e.g., 0.05 mL), followed by drying in laboratory air at 100 °C for 4 h. After this hydration treatment, the color of Mo^{VI}@*m*SiO_2 turned from white to yellow-green (i.e., the formation of $H_4SiMo_{12}O_{40}$ on silica). The catalysts synthesized from this process were simply named as $H_4SiMo_{12}O_{40}$@*m*SiO_2-*X*, where $X = 10$, 20, 30, and 40 are identical to the earlier denotations, although other phases might also be present in some cases apart from the targeted $H_4SiMo_{12}O_{40}$ compound. Commercial solid acid catalysts such as Amberlyst-15 and phosphomolybdic acid ($H_3PMo_{12}O_{40}$, PMA) were used as reference catalysts. 9%$H_4SiMo_{12}O_{40}$/SBA-15 was prepared by impregnation (i.e., an *outside-in* process) of SBA-15 support (synthesized according to literature method)[62] with ammonium heptamolybdate to achieve 9 wt % of Mo loading, followed by calcination at 500 °C for 3 h. After that 9%Mo/SBA-15 was hydrated with deionized water and dried at 100 °C for 4 h to yield 9%$H_4SiMo_{12}O_{40}$/SBA-15 (9 wt % of Mo loading). 9%PMA/SBA-15 was prepared by impregnation of SBA-15 with phosphomolybdic acid (9 wt % of Mo loading), followed by drying at 100 °C for 4 h. In addition to the $H_4SiMo_{12}O_{40}$@*m*SiO_2-*X*, for the comparison purpose, $H_4SiMo_{12}O_{40}$@*m*SiO_2 synthesized using 20 mg of smaller MoO_2 nanoparticles (∼20 nm) was denoted as $H_4SiMo_{12}O_{40}$@*m*SiO_2-20 nm.

Friedel−Crafts Benzylation of Toluene. Liquid phase Friedel−Crafts alkylation of toluene by benzyl alcohol was carried out in a three-necked round-bottom flask coupled with a reflux condenser in a temperature-controlled oil bath. In a typical experimental run, 50 mg of catalyst was added to a reactant mixture of 20.0 mL of toluene (C_7H_8, Tedia) and 0.5 mL of benzyl alcohol (C_7H_8O, Merck) with a small amount (0.1 mL) of tetradecane ($C_{14}H_{30}$, Alfa Aesar) used as an internal standard for GC analysis. The reaction was refluxed under vigorous magnetic stirring at 80 °C for various reaction times. The concentration of benzyl alcohol was monitored using gas chromatography (GC, Agilent-7890A) equipped with a flame ion detector (FID) and a HP-5 column (30 m × 0.32 mm ×0.25 μm). GC-mass spectrometer (GC−MS) was also employed to identify the reaction products.

Regeneration of Catalysts. The used catalyst was regenerated by thermal treatment at 500 °C for 3 h in static laboratory air. The calcined catalyst was similarly treated with 0.025 mL of deionized water, followed by drying at 100 °C for 4 h.

Materials Characterization. The crystallographic structure of the solid samples was investigated using powder X-ray diffraction (XRD, Bruker D8 Advance, Cu K_α radiation, $\lambda = 1.5406$ Å) at a scanning rate of 1°/min. The dimension, morphology, and chemical composition of the samples were examined using field emission scanning electron microscopy and energy dispersive X-ray spectroscopy (FESEM/EDX, JSM-6700F), transmission electron microscopy (TEM, JEM-2010, 200 kV), and high resolution transmission electron microscopy (HRTEM/EDX, JEM-2100F, 200 kV). The texture properties of the samples were studied by measuring nitrogen adsorption- desorption isotherms (Quantachrome NOVA-3000 system) at 77 K. Prior to measurements, the samples were degassed at 200 °C overnight. The specific surface areas of the samples were determined using Brunauer−Emmett−Teller (BET) method. The total pore volume was estimated at relative pressure from 0.928 to 0.936 of desorption curve. The pore size distribution was modeled using nonlocal density function theory (NLDFT) from adsorption curve.[63] Surface composition of the samples was investigated with X-ray photoelectron spectroscopy (XPS, AXIS-Hsi, Kratos Analytical) using a monochromatized Al K_α exciting radiation ($h\nu = 1486.71$ eV). The XPS spectra of all studied elements were measured with a constant analyzer-pass-energy of 40.0 eV. All binding energies (BEs) were referenced to the Si 2p peak (BE = 103.3 eV) from mesoporous silica phase. Chemical bonding information of the samples was acquired with Fourier transform infrared spectroscopy (FTIR, Bio-Rad FTS-135) using the potassium bromide (KBr) pellet technique. Furthermore, micro-Raman spectra were recorded with the 488 nm line of an Ar^+ laser excitation using a Jobin Yvon-T64000 micro-Raman system. The acidity of the above solid acid catalysts was determined by titration method.[64] Briefly, 0.2 g of solid catalyst was mixed with 10.0 mL of 3.42 M NaCl solution and stirred at room temperature for 30 h. After that, the solid-solution mixture was centrifuged and the filtrate was titrated by a 0.05 M NaOH solution. The equivalence point on the titration curve was used to calculate the acidity. ^{29}Si MAS spectrum was obtained at 79.49 MHz on a Bruker Advance 400 (DRX400) spectrometer. Sample was spun at a frequency of 8 kHz in Bruker 4 mm double-air-bearing CPMAS probe.

■ RESULTS AND DISCUSSION

Freestanding MoO_2 nanoparticles were first synthesized by a hydrothermal route using PVP as capping agent in a water−ethanol cosolvent, as shown in Figure 2a. The size distribution of MoO_2 nanoparticles was determined to be of 25 to 60 nm (Supporting Information, Figure S1). This synthetic route is effective and flexible. For example, to scale up the product of MoO_2 nanoparticles, the amount of ammonium heptamolybdate precursor could be simply increased from 150 mg (the standard amount reported in Experimental Section) to 200 mg or even 300 mg, without causing obvious changes of size and product morphology (Figure S2). The synthesis parameters, such as amounts of ammonium heptamolybdate, PVP and HCl, have been systematically explored in order to optimize the synthesis conditions (Figures S3−S8). Before used as cores for depositing silica shells, the as-prepared MoO_2 nanoparticles were washed with ethanol−acetone mixed solvent to remove excess of capping agent PVP. The deposition of silica shell on the MoO_2 core was carried out in water−ethanol cosolvent at room temperature, together with the surfactant CTACl. The water/ethanol ratio in this cosolvent system turned out to be an

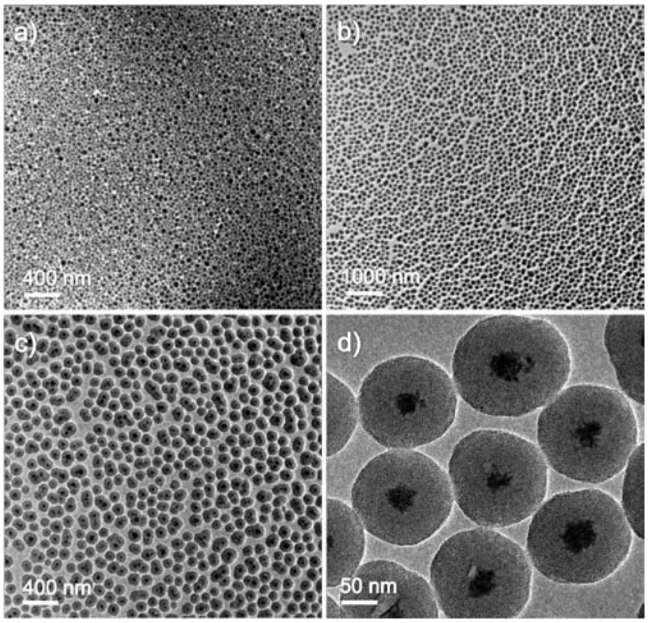

Figure 2. (a) TEM image of as-prepared MoO_2 nanoparticles, and (b-d) TEM images of $MoO_2@SiO_2$-20 core−shell spheres at different magnifications.

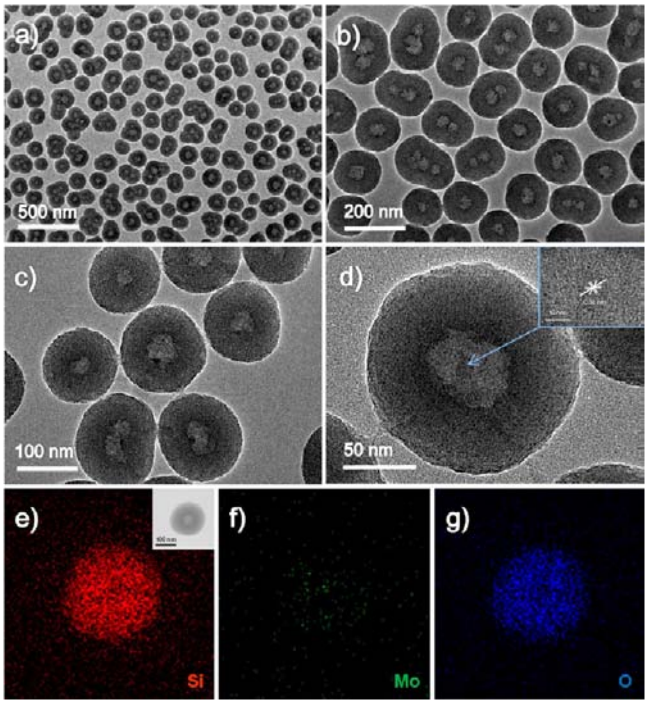

Figure 3. (a−d) TEM/HRTEM images of $Mo^{VI}@mSiO_2$-20 hollow spheres, and (e−g) EDX elemental mappings of a $Mo^{VI}@mSiO_2$-20 hollow sphere (see inserted TEM image in (e)).

important synthetic parameter to form uniform silica shells. In optimizing this volume ratio, the water/ethanol volume ratio was varied from 1.25 to 2.0, while keeping all other synthetic parameters unaltered. When the water/ethanol ratio was fixed at 1.25, the obtained $MoO_2@SiO_2$ core−shell nanospheres aggregated together. By increasing the water/ethanol ratio to 1.50, the dispersion of $MoO_2@SiO_2$ was improved significantly (Figure S9). At the volume ratio of water/ethanol =1.65, most of the core−shell spheres consisted of only one MoO_2 nanoparticle, though the spheres with two or three cores are also found occasionally. Further increasing this ratio to 2.0 resulted in coreless silica gel spheres (Figure S10). It is clear that the hydrolysis rate of TEOS was increased substantially when more water was used, leading to fast generation of silica nuclei. In such a case, some silica nuclei were still deposited onto the surface of MoO_2 spheres to form silica shells, while others simply aggregated into larger clusters and eventually precipitated out as the coreless pure silica. By optimizing the water/ethanol ratio in the range of 1.50−1.65, uniform silica shells could be successfully coated onto the MoO_2 nanoparticles, as reported in Figure 2b for a large scale panoramic view of the $MoO_2@SiO_2$. Under higher magnifications, in Figure 2c-d, the core−shell spheres as well as the mesoporous nature of silica shells become more obvious; the thickness of the silica shell is estimated to be around 50 nm (Figure 2d).

After a thermal treatment in static laboratory air at 550 °C for 6 h, the included CTACl was burned off. Rather unexpectedly, hollow cavities were generated within the mesoporous spheres, as displayed in Figure 3a-b. The encapsulated MoO_2 core spheres shrunk to less than 10 nm or even not observable in most spheres (Figure 3c,d). The inset in Figure 3d gives the HRTEM image of a tiny molybdenum oxide crystal left within the hollow cavity. The spacing of 0.34 nm is assigned to the lattice fringe of (040) plane of orthorhombic α-MoO_3 crystal structure (JCPDS card no. 05-0508, space group: *Pbnm*, $a_o = 3.962$ Å, $b_o = 13.85$ Å, and $c_o = 3.697$ Å). Therefore, it is believed that the previously encapsulated MoO_2 nanoparticles were oxidized to Mo^{VI} species (e.g., MoO_3 phase) and then infused into the mesopores silica shells which were also formed upon heating. To verify this postulation, EDX mapping was performed on individual $Mo^{VI}@mSiO_2$ hollow spheres (Figure 3e−g) as well as on a large group of such hollow spheres (Figure S11). On the basis of this investigation, it is confirmed that highly dispersed molybdenum (Mo^{VI}) species (which will also be detailed shortly) have been located inside the silica spheres. Arising from this metal loading process, moreover, the center of mesoporous silica spheres was also vacated. Such a hollow configuration is highly desirable for fast mass transfer of reactants and products when they are used as a catalyst, as mentioned earlier.

Shown in Figure 4a, crystallographic structures of MoO_2 (core) nanoparticles, $MoO_2@SiO_2$ core−shell spheres, and $Mo^{VI}@mSiO_2$ hollow spheres were further characterized by powder XRD technique. The crystalline phase of the oxide core nanoparticles can be assigned perfectly to monoclinic MoO_2 (JCPDS card no. 32-0671, space group: $P2_1/n$, $a_o = 5.606$ Å, $b_o = 4.859$ Å, and $c_o = 5.537$ Å). The XRD peaks become much weaker in the $MoO_2@SiO_2$ sample due to a low relative population of MoO_2 in this core−shell composite and possible etching of MoO_2 by the alkaline (TEA) during the formation of silica shells. After calcination in air at 550 °C for 6 h, no diffraction peaks of the resultant $Mo^{VI}@mSiO_2$ sample are detectable, since the total amount of MoO_3 residue is too small to be detected by the XRD technique (Figure 3d versus Figure 4a.iii). As mentioned earlier, it is believed that the major part of the oxidized molybdenum oxide was infused into the mesoporous shells at 550 °C. To prove this, XPS analysis was further employed in this study (Figure S12). Figure 4b gives the XPS spectrum of Mo 3d photoelectrons of $Mo^{VI}@mSiO_2$ hollow spheres. Deconvoluted Mo 3d doublet peaks

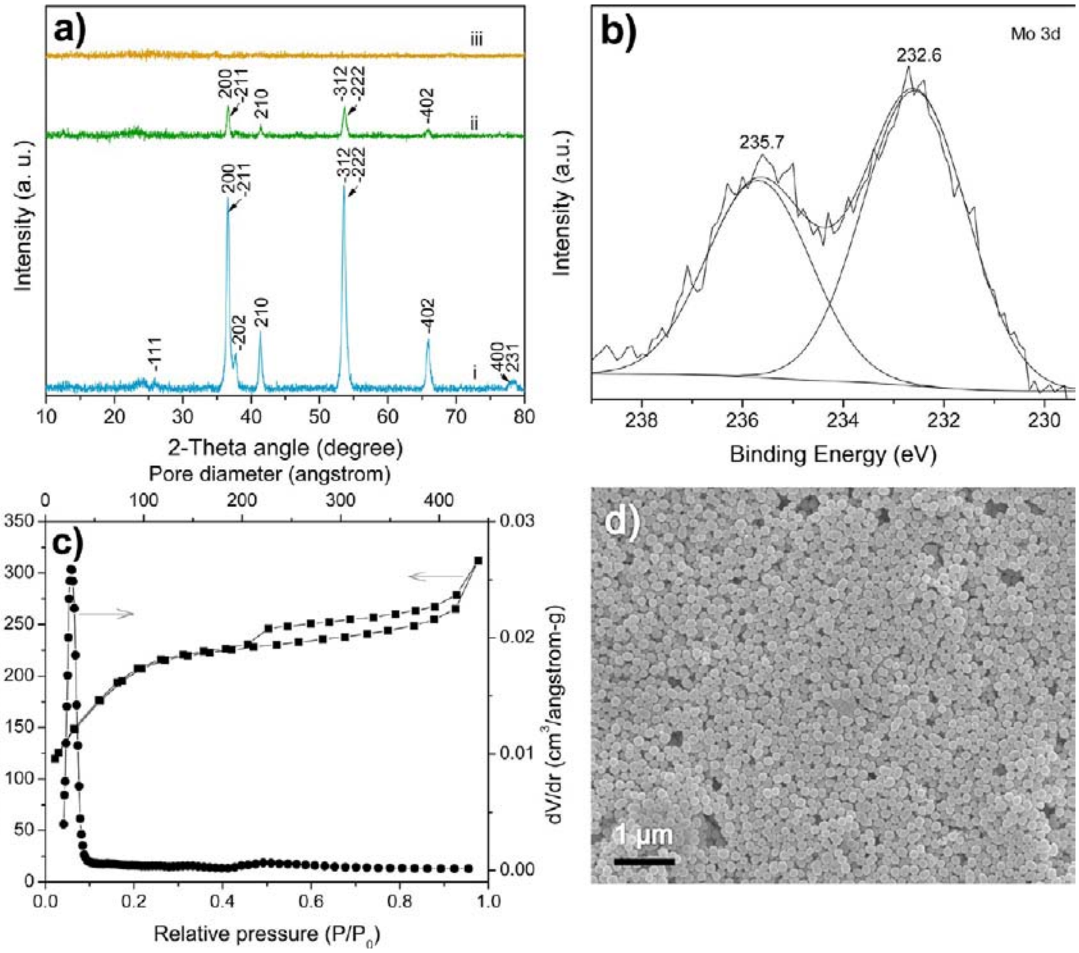

Figure 4. (a) XRD patterns of (i) MoO_2 nanoparticles, (ii) MoO_2@SiO_2-20 core−shell spheres, and (iii) Mo^{VI}@$m$$SiO_2$-20 hollow spheres; (b) X-ray photoelectron spectrum of Mo 3d; (c) N_2 adsorption−desorption isotherm and pore size distribution curve; and (d) FESEM image of Mo^{VI}@$m$$SiO_2$-20 hollow spheres.

suggest that molybdenum is solely in the state of Mo^{6+} (Mo $3d_{5/2}$ = 232.6 eV).[65,66] The textural properties of the Mo^{VI}@$m$$SiO_2$ sample was studied by nitrogen adsorption−desorption at 77 K, as shown in Figure 4c. The Mo^{VI}@$m$$SiO_2$ hollow spheres exhibit a type IV isotherm, which is typical for mesoporous silica synthesized with CTAB or CTACl as a surfactant. The corresponding hysteresis loop is type H4, which suggests the presence of narrow mesopores in the Mo^{VI}@$m$$SiO_2$ hollow spheres.[67] Indeed, the average pore size is very uniform and centered at around 2.6 nm, based on a NLDFT analysis with the data of adsorption branch. Figure 4d gives a large scale view of the Mo^{VI}@$m$$SiO_2$ product. The spheres are nearly monodisperse, and the average size of these hollow spheres is only around 100 nm. Therefore, the versatility of the current method is once again demonstrated.

Furthermore, the molybdenum loading could also be tuned facilely. In Figure 5a−c (Figures S13 and S14), with the weight of MoO_2 cores changed from 10 to 30 or 40 mg, the average size of the product MoO_2@SiO_2 nanospheres reduced from about 150 to 100 nm. This is understandable because less TEOS will be available for each MoO_2 nanoparticle when more MoO_2 cores are added but the supply of TEOS is kept constant. Consistent with this result, the thickness of the mesoporous silica shells was also reduced from about 60 to 40 nm in Figure 5d−f (Figures S15 and S16). After calcination, the overall size of the silica spheres remained unchanged exhibiting the stability of silica shells. In the sample of Mo^{VI}@$m$$SiO_2$-10, for example, the initial MoO_2 cores disappeared in almost all the spheres (Figure 5d). However, for the sample of Mo^{VI}@$m$$SiO_2$-30, the core component is still observable for some spheres under the same heat-treatment (Figure 5e) because more MoO_2 cores were included. The pore structures of the two samples were quite similar (Figure 5d,e). On the contrary, the pores of the sample Mo^{VI}@$m$$SiO_2$-40 seem to be expanded substantially (Figure 5f). Although there were no observable core oxide (MoO_3) particles within the hollow spheres, large MoO_3 nanorods were also found outside the silica spheres (TEM result, Figure S16). In this case, the silica shell was thinner but the initial molybdenum loading was higher (i.e., 40 mg). It is thus possible for the encapsulated molybdenum oxide to diffuse out of silica shells. Once the spontaneous nucleation occurred outside the silica spheres, forming thermodynamically stable monocrystalline MoO_3 nanorods became a viable option for Mo relocation (at 550 °C for 6 h). Of course, certain MoO_3 residue inside the spheres was still expected (which will be addressed shortly). In our present work, EDX analysis was carried out for each sample to determine the Mo loading on the hollow mesoporous silica spheres. The Mo/Si ratio before and after thermal treatment at 550 °C remained largely unchanged (Table S1), indicating that molybdenum was not lost due to evaporation. However, the MoO_3 nanorods were not observed in $H_4SiMo_{12}O_{40}$@$m$$SiO_2$-10, $H_4SiMo_{12}O_{40}$@$m$$SiO_2$-20, and

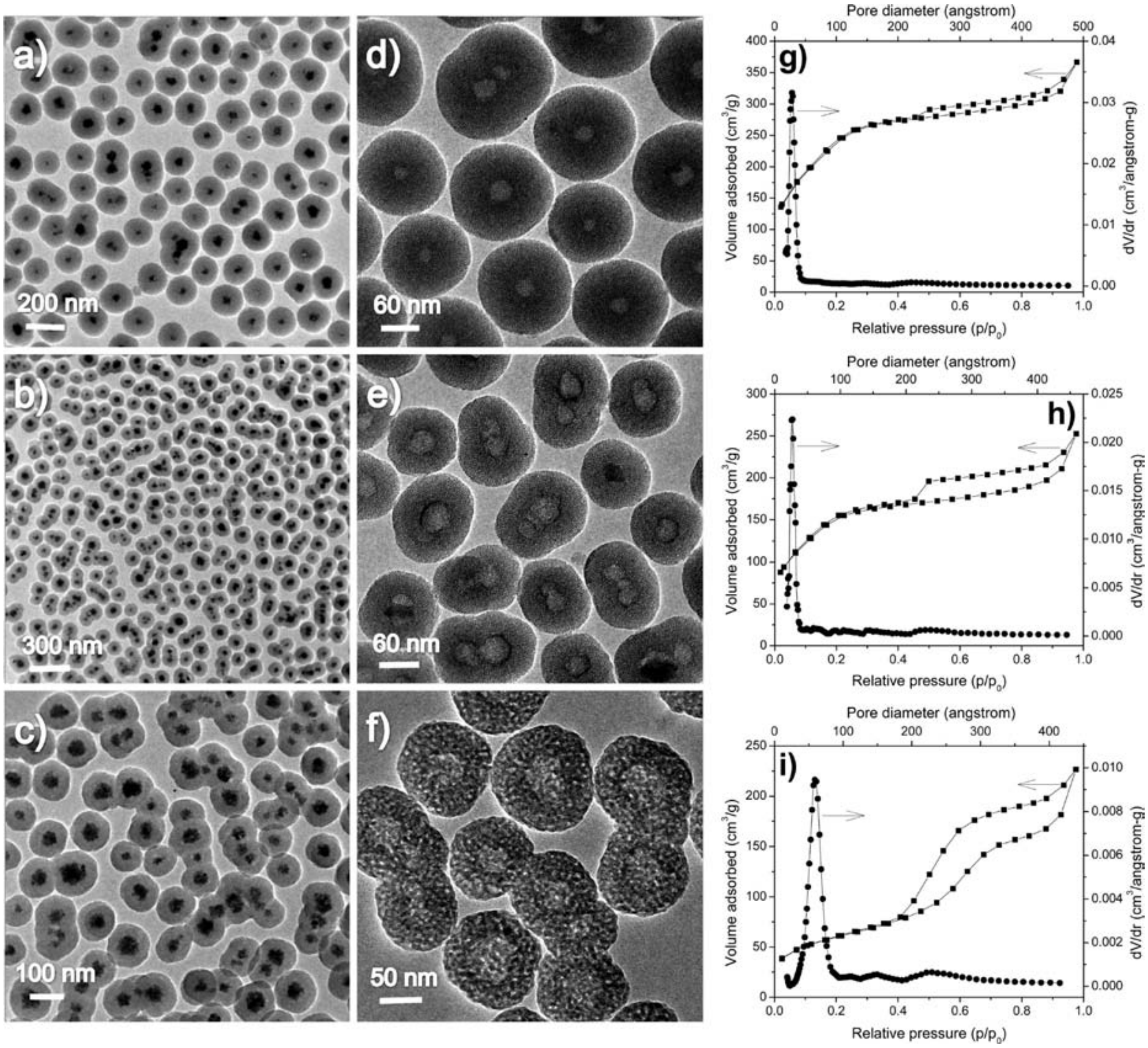

Figure 5. TEM images of (a) $MoO_2@SiO_2$-10, (b) $MoO_2@SiO_2$-30, (c) $MoO_2@SiO_2$-40, (d) $Mo^{VI}@mSiO_2$-10, (e) $Mo^{VI}@mSiO_2$-30, and (f) $Mo^{VI}@mSiO_2$-40; and N_2 adsorption−desorption isotherms and pore size distribution curves of (g) $Mo^{VI}@mSiO_2$-10, (h) $Mo^{VI}@mSiO_2$-30, and (i) $Mo^{VI}@mSiO_2$-40 hollow spheres.

$H_4SiMo_{12}O_{40}@$ $m$$SiO_2$-30 nanocatalysts. Assuming a maximum Mo content retained by silica spheres was 11 wt % (e.g., Mo content in $H_4SiMo_{12}O_{40}@mSiO_2$-30), the amount of α-MoO_3 nanorods coexisting in the sample of $H_4SiMo_{12}O_{40}@mSiO_2$-40 could be roughly estimated to be 5 wt % (i.e., 16 wt % − 11 wt %, Table 1). In Figure 5g−i, the texture properties of these $Mo^{VI}@mSiO_2$ hollow spheres are also reported. All the mesoporous samples exhibit type IV isotherms which can be associated with type H4 hysteresis loops (including the results of Figure 4c).[67] From Table 1, it is noted that the pore diameter remains as 2.6−2.8 nm at lower Mo loadings of 6−11 wt %, which increases drastically to 5.9 nm at the higher Mo loading of 16 wt %. Accordingly, the BET surface area dropped from 872 to 212 m^2/g. The significant change in pore size and surface area in the above sample series seemingly suggests increasing interactions between molybdenum and silica matrix, which will be addressed below. The small angle XRD patterns of $Mo^{VI}@mSiO_2$ hollow spheres show a broad peak around $2\theta = 1.4°$, which is associated with mesoporous silica having wormlike pore structures (Figure S17).[17]

Table 1. Physical Properties of the $Mo^{VI}@mSiO_2$-X (X = 10, 20, 30, and 40) Hollow Spheres with Different Mo Contents

catalyst	Mo content (wt %; EDX)	BET surface area (m^2/g)	pore volume (mL/g)	pore size (nm)
$Mo^{VI}@mSiO_2$-10	6	872	0.52	2.8
$Mo^{VI}@mSiO_2$-20	9	716	0.43	2.6
$Mo^{VI}@mSiO_2$-30	11	531	0.35	2.7
$Mo^{VI}@mSiO_2$-40	16	212	0.32	5.9

Reported in Figure 6, the crystallographic structure of the $Mo^{VI}@mSiO_2$-X hollow spheres was further investigated by XRD method. Consistent with the TEM observations, in particular, the $Mo^{VI}@mSiO_2$-10 and $Mo^{VI}@mSiO_2$-30 hollow spheres do not display any diffraction peaks of the MoO_3 phase, thus suggesting that either the resultant MoO_3 clusters might be too small to be detected or there were other molecular Mo^{VI} species anchored within the hollow spheres. On the contrary, very sharp diffraction peaks appearing at $2\theta = 12.7°$, 25.7° and 39.1° are observed in the sample of $Mo^{VI}@mSiO_2$-40; they correspond well to (020), (040), and (060) diffractions of

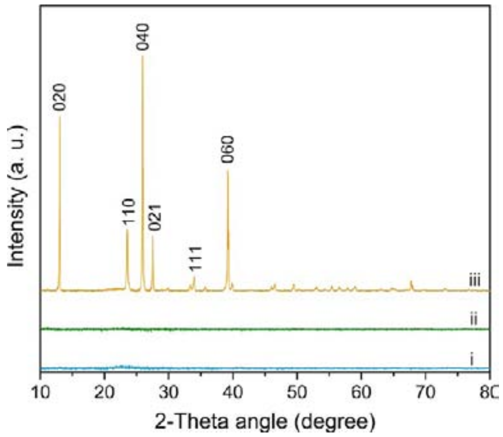

Figure 6. XRD patterns of (i) $Mo^{VI}@mSiO_2$-10, (ii) $Mo^{VI}@mSiO_2$-30, and (iii) $Mo^{VI}@mSiO_2$-40 hollow spheres.

orthorhombic α-MoO_3 phase (JCPDS card no. 05-0508, space group: *Pbnm*, $a_o = 3.962$ Å, $b_o = 13.85$ Å, and $c_o = 3.697$ Å). As revealed earlier, this is because of the formation of large α-MoO_3 nanorods in this high Mo-loading sample (TEM result, Figure S16).

The above $Mo^{VI}@mSiO_2$-*X* samples were hydrated with deionized water to synthesize the $H_4SiMo_{12}O_{40}$ (silicomolybdic acid) inside the porous spheres. Both the resultant $H_4SiMo_{12}O_{40}@ mSiO_2$ and its precursor $Mo^{VI}@mSiO_2$ were then tested as solid acid catalysts for Friedel−Crafts alkylation of toluene with benzyl alcohol (Figure 7a,b, and Table 2). Together, commercial solid acids such as Amberlyst-15, PMA, and PMA/SBA-15 were also used as benchmark catalysts in this evaluation (Table 2 and Figure S18). Among all the catalysts in Figure 7a, the $H_4SiMo_{12}O_{40}@mSiO_2$-20 was the most active, through which 94.7 and 99.7% of the initial benzyl alcohol was converted to methyl diphenylmethanes (1-methyl-2-(phenylmethyl) benzene, 1-methyl-3-(phenylmethyl)benzene, 1-methyl-4-(phenylmethyl)benzene), and dibenzyl ether (1,1′-[oxybis-(methylene)]bis-benzene, as a side product) at 80 and 120 min of the reaction (products identified by GC-MS as shown in Figures S19 and S20). It is noted that the selectivity of methyl diphenylmethanes in the total reaction products (methyl diphenylmethanes + dibenzyl ether) was 74 and 82% at 80 and 120 min respectively, which was further increased to 88% by prolonging the reaction to 180 min, indicating that dibenzyl ether can function as an alkylation agent as well. In comparison, the conversion of benzyl alcohol was 35.5 and 64.4% at 80 and 120 min accordingly using the commercial catalyst Amberlyst-15, that is the conversion % by $H_4SiMo_{12}O_{40}@mSiO_2$-20 is about 2.6 times as high as that by Amberlyst-15. It should be pointed out that Amberlyst-15 is one of the best solid acid catalysts for benzylation of toluene. Furthermore, our $H_4SiMo_{12}O_{40}@mSiO_2$-20 even has a comparable activity as

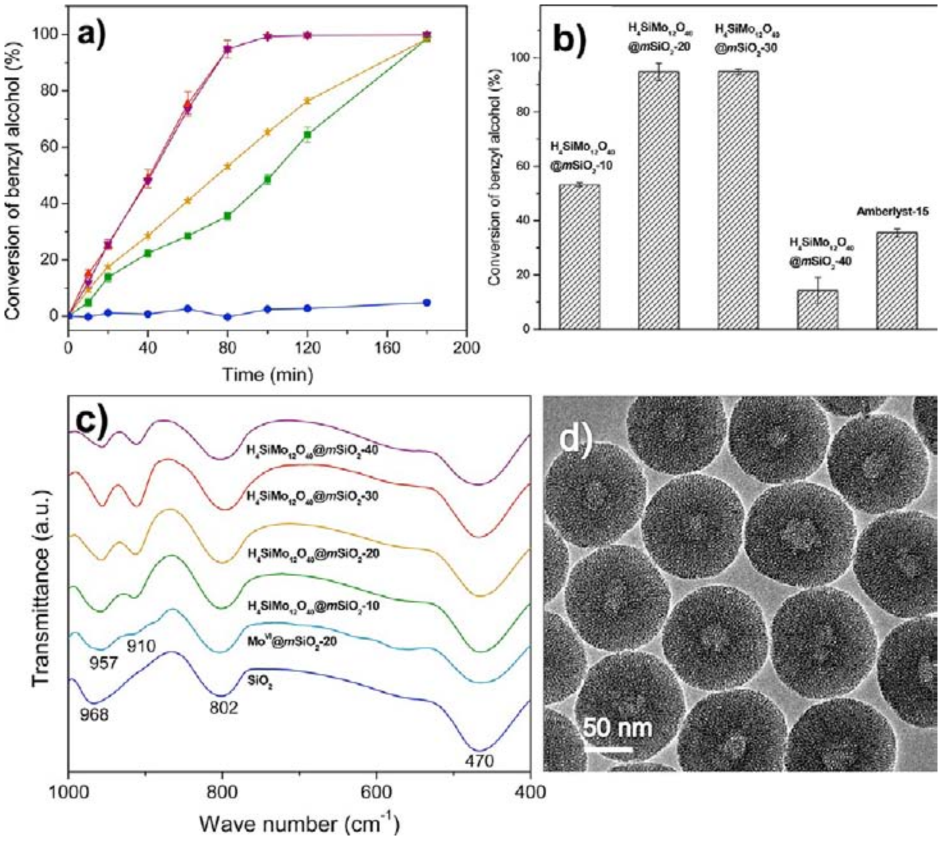

Figure 7. (a) Conversion of benzyl alcohol in Friedel−Crafts alkylation with $Mo^{VI}@mSiO_2$-20 (circle), Amberlyst-15 (square), $H_4SiMo_{12}O_{40}@mSiO_2$-10 (star), $H_4SiMo_{12}O_{40}@mSiO_2$-20 (triangle), and $H_4SiMo_{12}O_{40}@mSiO_2$-30 (triangle, upside down). For $Mo^{VI}@mSiO_2$-20 catalyst, the reaction was repeated twice. The rest reactions were all repeated 3 times. The error bar stands for the standard error in the three experiments; (b) Comparison of catalytic activities (at 80 min of reaction) of $H_4SiMo_{12}O_{40}@mSiO_2$-*X* (*X* = 10, 20, 30 and 40) with commercial solid acid catalyst Amberlyst-15; (c) IR spectra of $Mo^{VI}@mSiO_2$-20 and $H_4SiMo_{12}O_{40}@mSiO_2$-*X* (*X* = 10, 20, 30 and 40) hollow spheres, and pure silica and α-MoO_3 used as reference materials; and (d) TEM image of $H_4SiMo_{12}O_{40}@mSiO_2$-20 hollow spheres.

Table 2. Comparison of Friedel−Crafts Alkylation of Toluene over Solid Acid Catalysts[a]

catalyst	S_{BET} (m^2 g^{-1})	acidity[b] (mmol g^{-1})	yield[c] (%)	selectivity[d] (%)	activity[e] (mmol g^{-1} h^{-1})	TOF[f] (h^{-1})	TON[g]
$H_4SiMo_{12}O_{40}$@$m$$SiO_2$-10	701	0.13	31.5	26:3:31:40	38.5	296	391
$H_4SiMo_{12}O_{40}$@$m$$SiO_2$-20	620	0.26	69.0	33:4:38:25	68.6	264	486
$H_4SiMo_{12}O_{40}$@$m$$SiO_2$-30	445	N.D.	68.2	32:4:36:28	68.6	N.D.	N.D.
$H_4SiMo_{12}O_{40}$@$m$$SiO_2$-40	156	0.20	7.9	24:3:31:42	10.3	52	202
Amberlyst-15	45	3.50	15.3	18:2:23:57	25.7	8	270
9%$H_4SiMo_{12}O_{40}$/SBA-15	498	0.19	44.6	29:3:32:36	50.2	264	272
commercial PMA[i]	2	1.64[h]	23.4	33:4:32:31	24.6	15	N.D.
9%PMA/SBA-15	653	0.26	70.9	33:4:36:27	70.7	272	1430

Notes:

[a]Reaction conditions: toluene (20.0 mL), benzyl alcohol (0.5 mL), catalyst (50 mg), 80 °C. [b]Determined by titration method (see Experimental Section). [c]Yield was defined as alkylated products (*p*-, *m*-, and *o*-benzyl toluene) over initial benzyl alcohol at reaction time of 80 min. [d]Selectivity was defined as ratio of *o*-benzyl toluene:*m*-benzyl toluene:*p*-benzyl toluene:benzyl ether at reaction time of 80 min. [e]Activity was defined as mmol of benzyl alcohol converted per gram of catalyst per hour at reaction time of 80 min. [f]TOF was defined as number of benzyl alcohol molecules converted per acid site per hour at reaction time of 80 min. [g]TON (total number of benzyl alcohol molecules converted per acid site over a reaction period of 16 h) was determined by using the following reaction conditions: toluene (20.0 mL), benzyl alcohol (2.0 mL), catalyst (10 mg), 80 °C, 16 h. [h]Calculated from molecular formula $H_3PMo_{12}O_{40}$. [i]7 mg of PMA was used for Friedel−Crafts alkylation. N.D. - not determined.

commercial phosphomolybdic acid ($H_3PMo_{12}O_{40}$) supported on SBA-15 (i.e., 9%PMA/SBA-15, prepared by *outside-in* impregnation), with yields of alkylation products as 69.0% and 70.9% respectively (Table 2). It is known that the acid strength of $H_3PMo_{12}O_{40}$ is higher than $H_4SiMo_{12}O_{40}$,[39] thus the comparable activity could be due to better dispersion of $H_4SiMo_{12}O_{40}$ within mesoporous silica spheres using this *inside-out* strategy. In an additional comparison, 9%$H_4SiMo_{12}O_{40}$/SBA-15 prepared by *outside-in* impregnation could achieve only 44.6% yield of alkylation products at 80 min of reaction. The $H_4SiMo_{12}O_{40}$@ $m$$SiO_2$-10 catalyst, which had a lower Mo content, was also tested for the same alkylation reaction. About 53.2% conversion of benzyl alcohol was measured at 80 min, which is only one-half of that of the $H_4SiMo_{12}O_{40}$@$m$$SiO_2$-20. Nevertheless, it is still more active than Amberlyst-15, confirming again the superior activity of $H_4SiMo_{12}O_{40}$@ $m$$SiO_2$ toward Friedel−Crafts alkylation. The observed activity could be attributed to silicomolybdic acid formed after hydration, which is known as a strong heteropoly acid. As additional evidence, less than 5% conversion of benzyl alcohol was recorded for the nonhydrated Mo^{VI}@$m$$SiO_2$-20 catalyst (Figure 7a). The effect of the Mo loading on the catalytic activity is also compared in Figure 7b and Figure S21. The $H_4SiMo_{12}O_{40}$@$m$$SiO_2$-20 is the most active catalyst based on the weight of Mo metal or of the total catalyst, but a lower catalytic activity is observed in the $H_4SiMo_{12}O_{40}$@$m$$SiO_2$-10 since it has a lower content of Mo and less silicomolybdic acid is generated. Although the $H_4SiMo_{12}O_{40}$@$m$$SiO_2$-40 sample has the highest content of Mo, as explained earlier, a fraction of its molybdenum existed in the form of MoO_3 nanorods; the separated nanorods are apparently not as active as silicomolybdic acid. Furthermore, particle size of initial MoO_2 nanoparticles used in the synthesis seems to have negligible effect on the catalytic activity of the final catalyst, as $H_4SiMo_{12}O_{40}$@$m$$SiO_2$-20 nm shows similar conversion of benzyl alcohol as $H_4SiMo_{12}O_{40}$@ $m$$SiO_2$-20 (Figure 7a, and Figures S18 and S22).

Fourier-transform infrared spectra of $H_4SiMo_{12}O_{40}$@$m$$SiO_2$ and Mo^{VI}@$m$$SiO_2$ catalysts are presented in Figure 7c, where pure silica is also used as reference material. There are four IR bands observed for silica matrix. Bands at 1050−1250 (not shown, but similar to those in Figure 9b), 802, and 470 cm^{-1} could be assigned to asymmetric stretching, symmetric stretching, and bending modes of Si−O−Si linkages. The absorption peak at 968 cm^{-1} is due to stretching vibration of Si−OH bond in silica.[68] In addition to the Si−O−Si bands observed similar to pure silica, a broad band at 957 cm^{-1} was observed in the $H_4SiMo_{12}O_{40}$@$m$$SiO_2$-20 hollow spheres, which was attributed to terminal Mo=O vibration of surface polymeric molybdate phase.[69] On the other hand, a weak peak at 910 cm^{-1} could be assigned to Mo−O−Si vibration, which indicates strong chemical interaction between surface polymeric molybdate species and mesoporous silica shells.[69] After hydration treatment, the two peaks at 957 and 910 cm^{-1} became much more prominent, which was due to the formation of silicomolybdic acid,[57] especially in the samples of $H_4SiMo_{12}O_{40}$@$m$$SiO_2$-20 and $H_4SiMo_{12}O_{40}$@$m$$SiO_2$-30. It has been known that silicomolybdic acid can be generated by exposing silica-supported molybdenum oxide with moisture.[58] On the basis of this IR study, we verify that the silicomolybdic acid was synthesized in all our $H_4SiMo_{12}O_{40}$@$m$$SiO_2$ samples. Indirectly, we also validate the Mo^{VI}@$m$$SiO_2$ precursor proposed earlier, although the MoO_3 phase was not detectable by XRD.

It is noted that the morphology of hydrated hollow spheres remains essentially the same after the hydration, as shown in Figure 7d, noting that the molybdenum oxide species was transformed to silicomolybdic acid in this process (Figures S23 and S24). The structure of the hydrated samples was investigated by XRD method. The diffraction pattern is still amorphous (Figure S25), suggesting that either the molybdenum content is too low to be detected or the product $H_4SiMo_{12}O_{40}$ is noncrystalline. Thus, the surface composition of $H_4SiMo_{12}O_{40}$@$m$$SiO_2$ was also analyzed by XPS. Once again, the Mo 3d doublet peaks at 232.4 and 235.5 eV could be assigned solely to Mo^{6+} state (Figure S26), indicating that the oxidation state of molybdenum remained unchanged after the hydration. After hydration, BET surface areas decreased by 171 to 56 m^2/g for $H_4SiMo_{12}O_{40}$@ $m$$SiO_2$ hollow spheres (Table 1 versus Table 2, and Figure S27).

In order to obtain better confirmation on the presence of $H_4SiMo_{12}O_{40}$, Raman spectroscopic investigation was also conducted, because Raman spectroscopy is a sensitive technique to study supported metal oxide and it is complementary to IR investigation. The Raman spectra of the Mo^{VI}@$m$$SiO_2$ and its derived $H_4SiMo_{12}O_{40}$@$m$$SiO_2$ hollow

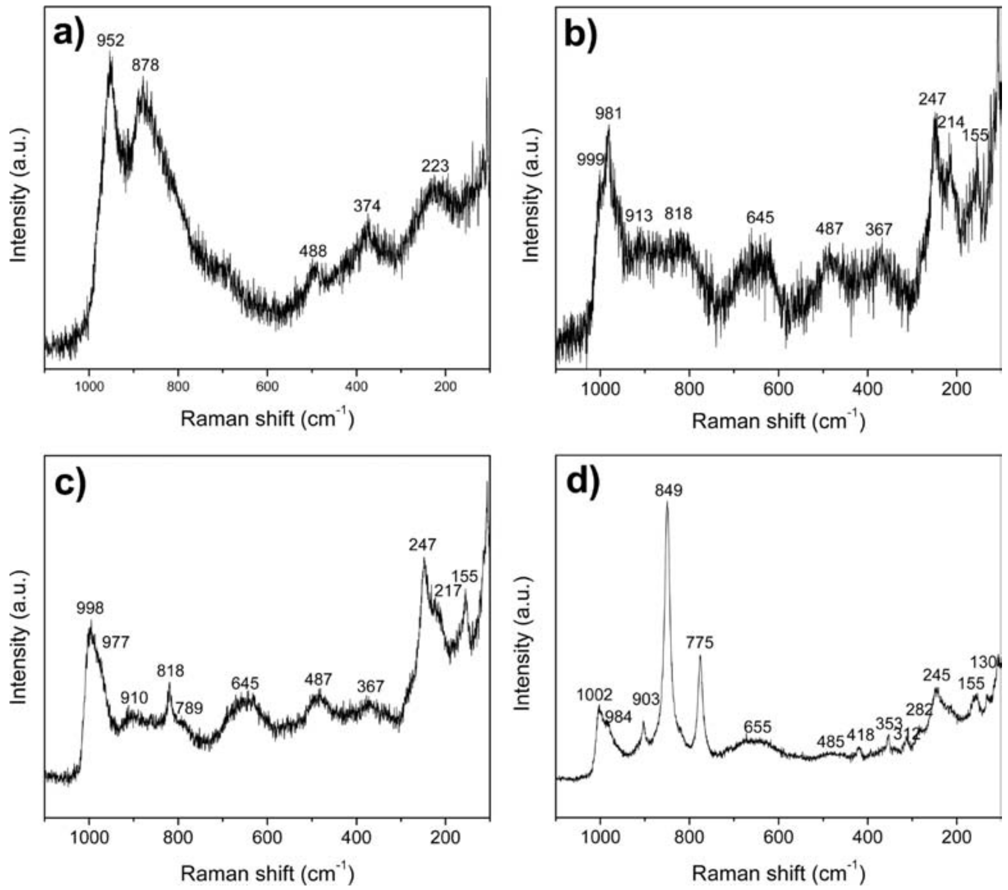

Figure 8. Raman spectra of (a) Mo^{VI}@$m$$SiO_2$-20, (b) $H_4SiMo_{12}O_{40}$@$m$$SiO_2$-10, (c) $H_4SiMo_{12}O_{40}$@$m$$SiO_2$-20, and (d) $H_4SiMo_{12}O_{40}$@$m$$SiO_2$-30 hollow spheres.

spheres are displayed in Figure 8, with reference to those of pure mesoporous silica and commercial α-MoO_3 (Figure S28). For pure mesoporous silica, the peak at 984 cm^{-1} is attributed to stretching vibration of Si−OH bond and the peak at 821 cm^{-1} to Si−O−Si linkages, while the two peaks at 648 and 487 cm^{-1} are assigned to the presence of siloxane rings (Figure S28).[70] Indeed, apart from the 488 cm^{-1} peak, there are four new peaks observed for the Mo^{VI}@$m$$SiO_2$-20 sample in Figure 8a, which are characteristic of heptamolybdate species ($Mo_7O_{24}^{6-}$).[71] The peaks at 952 and 878 cm^{-1} are due to symmetric and asymmetric stretching of the terminal Mo═O bond, while the peaks at 374 and 223 cm^{-1} are attributable to bending vibration of terminal Mo═O and deformation of Mo−O−Mo respectively.[71] It is noted that no peaks corresponding to the MoO_3 phase were observed, which indicates that the present thermal infusion method is effective to prepare highly dispersed molybdenum oxide within the mesoporous silica spheres. After the hydration of Mo^{VI}@$m$$SiO_2$ with water, more Raman peaks appeared due to restructuring of surface heptamolybdate species. The peaks at 998−999, 977−981, 910−913, 789, 645, and 247 cm^{-1} can be unambiguously assigned to silicomolybdic acid, though it is still difficult to differentiate between the α and β forms of this solid acid (Figure 8b,c).[58,72] In addition to those of silicomolybdic acid, the peaks at 818, 367 and 214−217, and 155 cm^{-1} are also observed; these peaks could be attributed to the presence of the α-MoO_3 phase. Quite clearly, water could also facilitate the crystallization of surface heptamolybdate species to small α-MoO_3 clusters, which probably took place during the drying process (100 °C). The above observation is also consistent with our FTIR findings, revealing that silicomolybdic acid is responsible for the high activity observed for the Friedel−Crafts alkylation. The higher activity of $H_4SiMo_{12}O_{40}$@$m$$SiO_2$-20 over $H_4SiMo_{12}O_{40}$@$m$$SiO_2$-10 is simply because this catalyst has a higher loading of Mo, which leads to a higher concentration of active silicomolybdic acid. Note that the Raman peak intensity of the $H_4SiMo_{12}O_{40}$@$m$$SiO_2$-20 is also stronger (Figure 8c versus Figure 8b). For the $H_4SiMo_{12}O_{40}$ @ $m$$SiO_2$-30 catalyst, however, only three peaks at 984, 655, and 245 cm^{-1} are observed corresponding to silicomolybdic acid (Figure 8d). Peaks at 1002, 282, 155, and 130 cm^{-1} are attributed to α-MoO_3 phase, while much sharper peaks at 903, 849, 775, 418, 353, and 312 cm^{-1} could be assigned to β-MoO_3 phase.[71,73] It is known that β-MoO_3 is only metastable,[74] while the α-MoO_3 is more stable at high temperature.[75,76] Because $H_4SiMo_{12}O_{40}$@$m$$SiO_2$-30 sample has a higher loading of molybdenum oxide compared to $H_4SiMo_{12}O_{40}$@$m$$SiO_2$-10 and $H_4SiMo_{12}O_{40}$ @$m$$SiO_2$-20, the drying at 100 °C for 4 h might not be sufficient to convert a larger amount of surface heptamolybdate species to the more stable α-MoO_3 phase. As a result, there is a mixture of both α- and β-MoO_3 phases in this sample. Though it has a higher Mo loading (11% Mo), the concentration of silicomolybdic acid in the $H_4SiMo_{12}O_{40}$@ $m$$SiO_2$-30 is likely to be about that of the $H_4SiMo_{12}O_{40}$@ $m$$SiO_2$-20, judging from relative intensities among the three phases (β-MoO_3 > α-MoO_3 > $H_4SiMo_{12}O_{40}$) in Figure 8d. Therefore, both samples exhibit very comparable activities (Figure 7b). Further increase in molybdenum content leads to

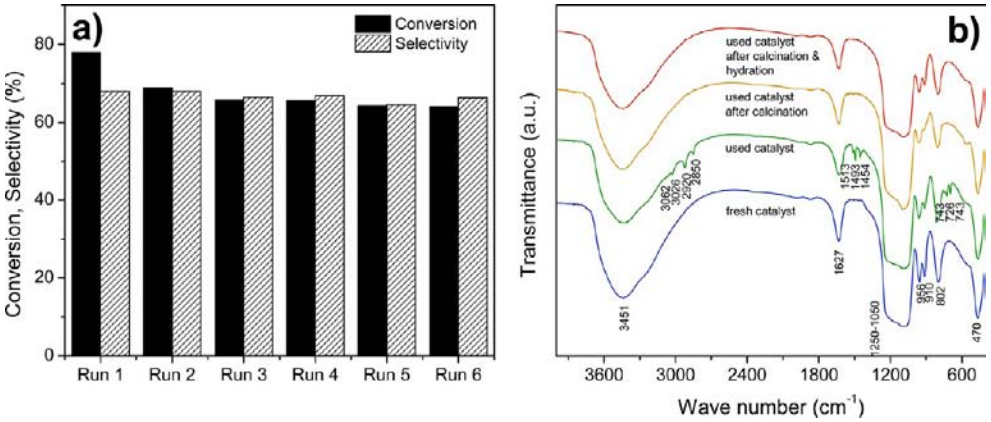

Figure 9. (a) Catalytic stability of hydrated $H_4SiMo_{12}O_{40}$@*m*SiO_2-20 catalyst is presented with conversion of benzyl alcohol and selectivity of alkylation products (defined as mol % of methyl diphenylmethanes in the total reaction products) after 60 min of reaction. (b) FTIR spectra of $H_4SiMo_{12}O_{40}$@*m*SiO_2-20 catalyst before and after reactions and under various regeneration treatment conditions.

the result of α-MoO_3 as a major phase (Figure S28) and the silicomolybdic acid peaks were no longer observable in Raman spectra, possibly being masked by strong peaks of α-MoO_3, although our IR study clearly indicates the presence of siliconmolybdic acid (Figure 7c) in the sample of $H_4SiMo_{12}O_{40}$@*m*SiO_2-40. Furthermore, ^{29}Si MAS NMR was carried out to characterize $H_4SiMo_{12}O_{40}$@*m*SiO_2-20 hollow spheres, as shown in Figure S29. At −76.5 ppm, a very tiny peak slightly above the background was observed, which can be assigned to $H_4SiMo_{12}O_{40}$ if it is truly a peak.[77] It has been reported in the literature that supported silicomolybdic acid or silicotungstic was not detectable by ^{29}Si NMR due to low concentration, though Raman spectra suggests the existence of these heteropoly acids.[77,78]

The catalytic stability of $H_4SiMo_{12}O_{40}$@*m*SiO_2-*X* has also been examined by recycling and regenerating used catalysts. In particular, in view of its good performance, the $H_4SiMo_{12}O_{40}$@*m*SiO_2-20 catalyst was chosen for this study. As shown in Figure 9a, the conversion of benzyl alcohol of the first run at 1 h was 77% which dropped to 68% in the second run and became quite steady in the following cycles (e.g., the conversion at the sixth run: 64%). Meanwhile, the selectivity of methyl diphenylmethanes over dibenzyl ether from the side reaction remained at ~66% for all 6 runs. It should be mentioned that the regeneration of used catalyst is essential to keep the high activity and selectivity. Without the regeneration, the catalyst was deactivated after 3 runs (Figure S30). The regeneration was carried out by thermal treatment of used catalyst at 500 °C in order to burn off any adsorbed organics, most likely the methyl diphenylmethanes. Shown in Figure 9b, the fresh, used, calcined, and regenerated catalysts were characterized by IR spectroscopy. For the fresh $H_4SiMo_{12}O_{40}$@*m*SiO_2-20, peaks at 3451 and 1627 cm^{-1} could be assigned to adsorbed water or surface −OH groups, while bands at 1050−1250, 802, and 470 cm^{-1} are attributed to silica matrix, as assigned earlier.[79] The two peaks at 956 and 910 cm^{-1} could be assigned to surface siliconmolybdic acid as mentioned in Figure 7c. After the reaction, there are some new peaks observed on the used catalyst. Peaks at 3062 and 3026 cm^{-1} are attributed to C−H stretch of aromatic compounds, while peaks at 2920 and 2850 cm^{-1} could be assigned to asymmetric and symmetric stretch of $-CH_2-$ (where the peak at 2920 cm^{-1} could be due to $-CH_3$ attached to aromatics as well),[79] which suggests that the used catalyst was adsorbed with alkylation products (i.e., methyl diphenylmethanes) and/or dibenzyl ether from the side reaction. Consistent with the above observations, peaks at 1513, 1493, and 1454 cm^{-1} can be assigned to carbon−carbon ring stretch, though the peak at 1454 could be due to scissoring of $-CH_2-$. The three small peaks at 743, 726, and 698 cm^{-1} of the far-IR range are due to wag of aromatic C−H.[79] It is noted that the asymmetric stretch of C−O−C at ~1100 cm^{-1} could be well masked by the broad SiO_2 band at 1050−1250 cm^{-1}. After the thermal treatment of the used catalyst at 500 °C, the adsorbed organic compounds were removed, as the peaks due to C−H or $-CH_2-$ all disappeared. In addition, the peak at 910 cm^{-1} was also significantly weakened, possibly due to decomposition of surface silicomolybdic acid, as it is not stable above 400 °C. After the hydration treatment, this heteropoly acid was restored as evidenced in the reappearing peak at 910 cm^{-1}.

■ CONCLUSIONS

In summary, we have developed a facile hydrothermal method to prepare free-standing MoO_2 nanoparticles with sizes in the range of 25−60 nm, which were then used as cores to be coated with a uniform CTACl-templated silica shell. By varying the amount of MoO_2 cores used, the diameter of MoO_2@SiO_2 core−shell spheres could be tuned from 100 to 150 nm. After thermal treatment of as-prepared MoO_2@SiO_2 at 550 °C in air, the templating molecules (CTACl) were burned off, and mesoporous Mo^{VI}@*m*SiO_2 products were generated, which have a specific surface area from 212 to 872 m^2/g and pore-size distribution from 5.9 to 2.6 nm, depending on the initial MoO_2 cores used in the synthesis. During the same process, the encapsulated MoO_2 nanocrystals were oxidized to Mo^{VI} and diffused outward to mesoporous silica shells, leaving a void space at the center of mesoporous silica spheres. The oxidized molybdenum existed as heptamolybdate species ($Mo_7O_{24}^{6-}$) on the silica mesopore surface, which was later transformed into silicomolybdic acid ($H_4SiMo_{12}O_{40}$) by interaction with silica shells in the presence of water. It was noted that, apart from heteropoly acid $H_4SiMo_{12}O_{40}$, β- and/or α-MoO_3 could also be present (if desired), depending on the initial molybdenum loading. Because this is an *inside-out* synthesis for catalysts, blockage in the pore entrance can be avoided. The $H_4SiMo_{12}O_{40}$-anchored mesoporous silica hollow spheres were demonstrated to be highly active for Friedel−Crafts alkylation. The best two catalysts screened, $H_4SiMo_{12}O_{40}$@

mSiO$_2$-20 and $H_4SiMo_{12}O_{40}$@mSiO$_2$-30, were approximately 2.6 times as active as the commercial Amberlyst-15 solid acid catalyst, with 99% conversion of benzyl alcohol to methyl diphenylmethanes and dibenzyl ether within 90 min at the reaction temperature of 80 °C. More importantly, the $H_4SiMo_{12}O_{40}$@mSiO$_2$ hollow sphere catalyst was robust, which could be reused after regeneration. Conversion of benzyl alcohol and selectivity of methyl diphenylmethanes over dibenzyl ether were maintained at 64 and 66%, respectively, after six runs of repeated experiments. Catalyst regeneration was performed to burn off reaction products adsorbed and restore the active silicomolybdic acid species. The present preinstallation−infusion−hydration method could be applied to prepare highly dispersed metal oxides on mesoporous supports, while generating hollow structures. In addition, the developed $H_4SiMo_{12}O_{40}$@mSiO$_2$ hollow spheres can also be used as solid acid support to prepare bifunctional catalysts for wide applications.[80,81]

■ ASSOCIATED CONTENT

Ⓢ Supporting Information

TEM images, EDX mapping, XPS spectra, GC−MS spectra, XRD, N_2 adsorption−desorption isotherms and pore size distributions, pH titration curves, Raman spectra, ^{29}Si MAS spectrum, and recycle test. This material is available free of charge via the Internet at http://pubs.acs.org.

■ AUTHOR INFORMATION

Corresponding Author

chezhc@nus.edu.sg

Notes

The authors declare no competing financial interest.

■ ACKNOWLEDGMENTS

The authors gratefully acknowledge the financial supports provided by the National University of Singapore, and GSK, Singapore.

■ REFERENCES

(1) Wan, Y.; Zhao, D. Y. *Chem. Rev.* **2007**, *107*, 2821−2860.

(2) Kresge, C. T.; Leonowicz, M. E.; Roth, W. J.; Vartuli, J. C.; Beck, J. S. *Nature* **1992**, *359*, 710−712.

(3) Zhao, D. Y.; Feng, J. L.; Huo, Q. S.; Melosh, N.; Fredrickson, G. H.; Chmelka, B. F.; Stucky, G. D. *Science* **1998**, *279*, 548−552.

(4) Grun, M.; Kurganov, A. A.; Schacht, S.; Schuth, F.; Unger, K. K. *J. Chromatogr., A* **1996**, *740*, 1−9.

(5) Mercier, L.; Pinnavaia, T. J. *Adv. Mater.* **1997**, *9*, 500−503.

(6) Mal, N. K.; Fujiwara, M.; Tanaka, Y. *Nature* **2003**, *421*, 350−353.

(7) Lee, J. E.; Lee, N.; Kim, T.; Kim, J.; Hyeon, T. *Acc. Chem. Res.* **2012**, *44*, 893−902.

(8) Moller, K.; Bein, T. *Chem. Mater.* **1998**, *10*, 2950−2963.

(9) Taguchi, A.; Schuth, F. *Microporous Mesoporous Mater.* **2005**, *77*, 1−45.

(10) Sayari, A.; Hamoudi, S. *Chem. Mater.* **2001**, *13*, 3151−3168.

(11) Brunel, D. *Microporous Mesoporous Mater.* **1999**, *27*, 329−344.

(12) Wang, D. P.; Zeng, H. C. *Chem. Mater.* **2011**, *23*, 4886−4899.

(13) Guerrero-Martinez, A.; Perez-Juste, J.; Liz-Marzan, L. M. *Adv. Mater.* **2010**, *22*, 1182−1195.

(14) Joo, S. H.; Park, J. Y.; Tsung, C. K.; Yamada, Y.; Yang, P. D.; Somorjai, G. A. *Nat. Mater.* **2009**, *8*, 126−131.

(15) Kim, J.; Lee, J. E.; Lee, J.; Yu, J. H.; Kim, B. C.; An, K.; Hwang, Y.; Shin, C. H.; Park, J. G.; Kim, J.; Hyeon, T. *J. Am. Chem. Soc.* **2006**, *128*, 688−689.

(16) Zhao, W. R.; Gu, J. L.; Zhang, L. X.; Chen, H. R.; Shi, J. L. *J. Am. Chem. Soc.* **2005**, *127*, 8916−8917.

(17) Moller, K.; Kobler, J.; Bein, T. *Adv. Funct. Mater.* **2007**, *17*, 605−612.

(18) Lin, H.-P.; Cheng, Y.-R.; Mou, C.-Y. *Chem. Mater.* **1998**, *10*, 3772−3776.

(19) Zeng, H. C. *J. Mater. Chem.* **2011**, *21*, 7511−7526.

(20) Li, J.; Zeng, H. C. *J. Am. Chem. Soc.* **2007**, *129*, 15839−15847.

(21) Yang, H. G.; Zeng, H. C. *J. Phys. Chem. B* **2004**, *108*, 3492−3495.

(22) Caruso, F.; Caruso, R. A.; Mohwald, H. *Science* **1998**, *282*, 1111−1114.

(23) Zhu, Y. F.; Shi, J. L.; Shen, W. H.; Dong, X. P.; Feng, J. W.; Ruan, M. L.; Li, Y. S. *Angew. Chem., Int. Ed.* **2005**, *44*, 5083−5087.

(24) Wang, J. G.; Li, F.; Zhou, H. J.; Sun, P. C.; Ding, D. T.; Chen, T. H. *Chem. Mater.* **2009**, *21*, 612−620.

(25) Rana, R. K.; Mastai, Y.; Gedanken, A. *Adv. Mater.* **2002**, *14*, 1414−1418.

(26) Kim, S. S.; Zhang, W. Z.; Pinnavaia, T. J. *Science* **1998**, *282*, 1302−1305.

(27) Schacht, S.; Huo, Q.; Voigt-Martin, I. G.; Stucky, G. D.; Schuth, F. *Science* **1996**, *273*, 768−771.

(28) Qi, G. G.; Wang, Y. B.; Estevez, L.; Switzer, A. K.; Duan, X. N.; Yang, X. F.; Giannelis, E. P. *Chem. Mater.* **2010**, *22*, 2693−2695.

(29) Tan, B.; Rankin, S. E. *Langmuir* **2005**, *21*, 8180−8187.

(30) Chen, Y.; Chen, H. R.; Guo, L. M.; He, Q. J.; Chen, F.; Zhou, J.; Feng, J. W.; Shi, J. L. *ACS Nano* **2010**, *4*, 529−539.

(31) Busca, G. *Chem. Rev.* **2007**, *107*, 5366−5410.

(32) Chiu, J. J.; Pine, D. J.; Bishop, S. T.; Chmelka, B. F. *J. Catal.* **2004**, *221*, 400−412.

(33) Dou, J.; Zeng, H. C. *J. Phys. Chem. C* **2012**, *116*, 7767−7775.

(34) Tagusagawa, C.; Takagaki, A.; Iguchi, A.; Takanabe, K.; Kondo, J. N.; Ebitani, K.; Hayashi, S.; Tatsumi, T.; Domen, K. *Angew. Chem., Int. Ed.* **2010**, *49*, 1128−1132.

(35) Wang, F.; Ueda, W. *Chem.—Eur. J.* **2009**, *15*, 742−753.

(36) Suganuma, S.; Nakajima, K.; Kitano, M.; Yamaguchi, D.; Kato, H.; Hayashi, S.; Hara, M. *J. Am. Chem. Soc.* **2008**, *130*, 12787−12793.

(37) Rao, Y.; Trudeau, M.; Antonelli, D. *J. Am. Chem. Soc.* **2006**, *128*, 13996−13997.

(38) Okuhara, T. *Chem. Rev.* **2002**, *102*, 3641−3665.

(39) Kozhevnikov, I. V. *Chem. Rev.* **1998**, *98*, 171−198.

(40) Corma, A. *Chem. Rev.* **1995**, *95*, 559−614.

(41) Liu, F. J.; Willhammar, T.; Wang, L.; Zhu, L. F.; Sun, Q.; Meng, X. J.; Carrillo-Cabrera, W.; Zou, X. D.; Xiao, F.-S. *J. Am. Chem. Soc.* **2012**, *134*, 4557−4560.

(42) Na, K.; Jo, C.; Kim, J; Cho, K.; Jung, J.; Seo, Y.; Messinger, R. J.; Chmelka, B. F.; Ryoo, R. *Science* **2011**, *333*, 328−332.

(43) Chen, H. Y.; Wydra, J.; Zhang, X. Y.; Lee, P.-S.; Wang, Z. P.; Fan, W.; Tsapatsis, M. *J. Am. Chem. Soc.* **2011**, *133*, 12390−12393.

(44) Moller, K.; Yilmaz, B.; Jacubinas, R. M.; Muller, U.; Bein, T *J. Am. Chem. Soc.* **2011**, *133*, 5284−5295.

(45) Gu, F. N.; Wei, F.; Yang, J. Y.; Lin, N.; Lin, W. G.; Wang, Y.; Zhu, J. H. *Chem. Mater.* **2010**, *22*, 2442−2450.

(46) Perez-Ramirez, J.; Christensen, C. H.; Egeblad, K.; Christensen, C. H.; Groen, J. C. *Chem. Soc. Rev.* **2008**, *37*, 2530−2542.

(47) Okuhara, T.; Mizuno, N.; Misono, M. *Appl. Catal., A* **2001**, *222*, 63−77.

(48) Verhoef, M. J.; Kooyman, P. J.; Peters, J. A.; van Bekkum, H. *Microporous Mesoporous Mater.* **1999**, *27*, 365−371.

(49) Blasco, T.; Corma, A.; Martinez, A.; Martinez-Escolano, P. *J. Catal.* **1998**, *177*, 306−313.

(50) Liu, Y.; Xu, L.; Xu, B. B.; Li, Z. K.; Jia, L. P.; Guo, W. G. *J. Mol. Catal. A: Chem.* **2009**, *297*, 86−92.

(51) Zhu, Z. R.; Yang, W. M. *J. Phys. Chem. C* **2009**, *113*, 17025−17031.

(52) Nowinska, K.; Formaniak, R.; Kaleta, W.; Waclaw, A. *Appl. Catal., A* **2003**, *256*, 115−123.

(53) Lapkin, A.; Bozkaya, B.; Mays, T.; Borello, L.; Edler, K.; Crittenden, B. *Catal. Today* **2003**, *81*, 611−621.

(54) Zhang, R. F.; Yang, C. *J. Mater. Chem.* **2008**, *18*, 2691−2703.

(55) Dufaud, V.; Lefebvre, F.; Niccolai, G. P.; Aouine, M. *J. Mater. Chem.* **2009**, *19*, 1142−1150.

(56) Jalil, P. A.; Faiz, M.; Tabet, N.; Hamdan, N. M.; Hussain, Z. *J. Catal.* **2003**, *217*, 292−297.

(57) Rocchiccioli-Deltcheff, C.; Amirouche, M.; Fournier, M. *J. Catal.* **1992**, *138*, 445−456.

(58) Banares, M. A.; Hu, H. C.; Wachs, I. E. *J. Catal.* **1995**, *155*, 249−255.

(59) Piao, Y.; Kim, J.; Na, H. B.; Kim, D.; Baek, J. S.; Ko, M. K.; Lee, J. H.; Shokouhimehr, M.; Hyeon, T. *Nat. Mater.* **2008**, *7*, 242−247.

(60) Shin, J.; Kim, H.; Lee, I. S. *Chem. Commun.* **2008**, 5553−5555.

(61) Park, J. C.; Lee, H. J.; Bang, J. U.; Park, K. H.; Song, H. *Chem. Commun.* **2009**, 7345−7347.

(62) Luan, Z. H.; Hartmann, M.; Zhao, D. Y.; Zhou, W. Z.; Kevan, L. *Chem. Mater.* **1999**, *11*, 1621−1627.

(63) Ravikovitch, P. I.; Domhnaill, S. C. O.; Neimark, A. V.; Schuth, F.; Unger, K. K. *Langmuir* **1995**, *11*, 4765−4772.

(64) Lopez, D. E.; Goodwin, J. G., Jr; Bruce, D. A. *J. Catal.* **2007**, *245*, 381−391.

(65) Okamoto, Y.; Imanaka, T.; Teranishi, S. *J. Phys. Chem.* **1981**, *85*, 3798−3805.

(66) Banares, M. A.; Fierro, J. L. G.; Moffat, J. B. *J. Catal.* **1993**, *142*, 406−417.

(67) Sing, K. S. W.; Everett, D. H.; Haul, R. A. W.; Moscou, L.; Pierotti, R. A.; Rouquerol, J.; Siemieniewska, T. *Pure Appl. Chem.* **1985**, *57*, 603−619.

(68) El Shafei, G. M. S.; Mokhtar, M. *Colloid Surf. A* **1995**, *94*, 267−277.

(69) Seyedmonir, S. R.; Abdo, S.; Howe, R. F. *J. Phys. Chem.* **1982**, *86*, 1233−1235.

(70) Hu, H. C.; Wachs, I. E.; Bare, S. R. *J. Phys. Chem.* **1995**, *99*, 10897−10910.

(71) Banares, M. A.; Hu, H. C.; Wachs, I. E. *J. Catal.* **1994**, *150*, 407−420.

(72) Kasprzak, M. S.; Leroi, G. E.; Crouch, S. R. *Appl. Spectrosc.* **1982**, *36*, 285−289.

(73) Dieterle, M.; Mestl, G. *Phys. Chem. Chem. Phys.* **2002**, *4*, 822−826.

(74) Wei, X. M.; Zeng, H. C. *J. Phys. Chem. B* **2003**, *107*, 2619−2622.

(75) Wei, X. M..; Zeng, H. C. *Chem. Mater.* **2003**, *15*, 433−442.

(76) Yang, H. G.; Zeng, H. C. *Chem. Mater.* **2003**, *15*, 3113−3120.

(77) Piquemal, J. Y.; Briot, E.; Chottard, G.; Tougne, P.; Manoli, J. M.; Bregeault, J. M. *Microporous Mesoporous Mater.* **2003**, *58*, 279−289.

(78) Sawant, D. P.; Vinu, A.; Mirajkar, S. P.; Lefebvre, F.; Ariga, K.; Anandan, S.; Mori, T.; Nishimura, C.; Halligudi, S. B. *J. Mol. Catal. A: Chem.* **2007**, *271*, 46−56.

(79) Patnaik, P. *Dean's Analytical Chemistry Handbook*; McGraw-Hill: New York, 2004.

(80) Shiju, N. R.; Alberts, A. H.; Khalid, S.; Brown, D. R.; Rothenberg, G. *Angew. Chem., Int. Ed.* **2011**, *50*, 9615−9619.

(81) Huang, Y. L.; Xu, S.; Lin, V. S.-Y. *Angew. Chem., Int. Ed.* **2011**, *50*, 661−664.